

## Research Article

# Experiment and Analysis of Cord Stress on High-Speed Radial Tire Standing Waves

Peng-Fei Sun <sup>1,2</sup> Hong-Wu Huang <sup>1,2</sup> Shui-Ting Zhou <sup>2</sup> Yi-Jui Chiu,<sup>2</sup> Meng Du,<sup>2</sup>  
and Dong-Hao Zhao <sup>2</sup>

<sup>1</sup>School of Aerospace Engineering, Xiamen University, Xiamen 361005, China

<sup>2</sup>Collaborative Innovation Center for R&D of Coach and Special Vehicle, Xiamen University of Technology, 361024 Xiamen, Fujian, China

Correspondence should be addressed to Hong-Wu Huang; hhw6796@xmut.edu.cn

Received 21 May 2019; Accepted 3 July 2019; Published 30 July 2019

Academic Editor: Marco Tarabini

Copyright © 2019 Peng-Fei Sun et al. This is an open access article distributed under the Creative Commons Attribution License, which permits unrestricted use, distribution, and reproduction in any medium, provided the original work is properly cited.

This paper elaborates on the production mechanisms of standing waves during high-speed tire rolling and analyzes the relationship between the change of wavelength of sidewall waves and the vehicle velocity, from an oblique wave point of view. A finite element model for a 195/65R15 radial tire is established with the nonlinear analysis software ABAQUS, based on the tire structure and cord parameters. This paper comparatively analyzes the finite element simulation results and experimental results of the tire load-sinkage relation and the load vs inflatable section width relation and finds little difference between the simulation and experimental results. A similar analysis studies the change in the wavelength of sidewall standing waves at different vehicle velocities during high-speed tire rolling. The calculated value by the oblique wave approach, the value by simulation, and the experimental results demonstrate high consistency, concluding that during high-speed tire rolling, the wavelength of sidewall standing waves increases with vehicle velocity. Thus, the accuracy of the finite element model is verified under both static and dynamic conditions. Under a constant tire pressure and load, the impact of velocity change on tire-cord stress during high-speed tire rolling is studied based on the finite element model so as to identify the relation between the cord stress and standing waves.

## 1. Introduction

Traffic accidents caused by tire bursts occur frequently, and studies have found that the standing wave on high-speed tires is a major cause of tire bursts. The weight of a vehicle causes a slight deformation of a tire where it contacts the ground, and the deformed part tends to regain its original shape after rolling out of ground contact. When a vehicle moves at a high speed, the tire rolls too fast to regain its original shape from deformation, thereby forming standing waves [1], as shown in Figure 1. The speed at which standing waves are generated is referred to as the critical speed of the tire. A tire tread on which standing waves are generated rapidly heats up due to intense friction in this state, which can strip tread rubber from the inner carcass and cause a tire burst. The higher the velocity of the tire, the more obvious the standing wave [2].

High-performance computers, high-speed cameras, and high-power chassis dynamometers have been increasingly used to explore the mechanisms that produce standing waves in tires. Brockman [3] presented a semianalytical finite element method to analyze and solve the critical speed for standing waves in pneumatic tires. Since this method accounts for tire expansion and vibration-rotation superposition, it has high accuracy. Chatterjee [4, 5] carried out experiments on small-diameter tires and found that (1) standing waves occur at a certain critical speed and the tire radial displacement increases with increasing speed and (2) the standing wave phenomenon is most obvious when part of a tire rolls immediately out of ground contact and attenuates rapidly in the circumferential direction of the tire. Chang et al. [6] utilized PAM-SHOCK finite element software to simulate the process when the tire velocity increased from 0 to 300 km/h within 0.6 seconds, obtaining the critical

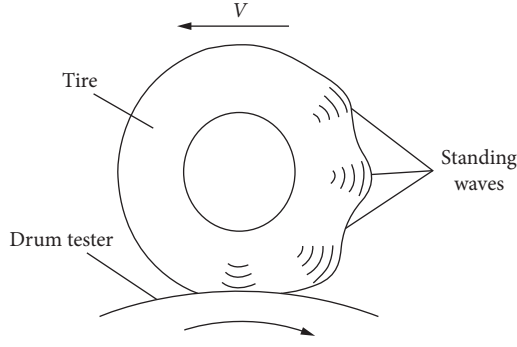


FIGURE 1: Tire standing waves.

speed for standing wave generation. According to Chang, both the tire inflation pressure and load have a great impact on the critical speed. In addition, from Chang's point of view, standing waves are not resonances; they are caused by residual stress and deformation of the ground contact part, which cannot immediately regain its original shape due to high-speed rolling [7].

This paper analyzes the production mechanisms of standing waves during high-speed tire rolling and the changes of wavelength on the sidewall based on the oblique wave approach. ABAQUS is used to establish a three-dimensional finite element model of the tire and drum tester, and both static and dynamic experiments are carried out to verify the accuracy of the finite element model. Furthermore, the paper analyzes how the cord stress changes with the vehicle velocity during high-speed tire rolling and discusses the mechanical patterns of tire standing waves, providing a mechanical basis for tire design so as to improve tire safety and service life.

## 2. Diagonal Wave Theory

Diagonal waves can be considered as waves transmitted in pipes or plane waves transmitted in the waveguide with a certain angle, frequency, and width [8]. When waves are transmitted on a uniformly stretched flexible film, the film has rigid boundaries in the longitudinal ( $X$ ) and transverse ( $Y$ ) directions. The transmission velocity of the plane waves on the film is  $C = \sqrt{T/\rho}$ , where  $T$  is the force per unit length and  $\rho$  is the mass per unit area. If the two plane waves are transmitted to the  $X$ -axis at the same angle  $\theta$ , a series of symmetric peaks and troughs will be transmitted along the centerline of the film [9]. Figure 1 demonstrates a fundamental wave, in which the entire tire section alternately moves outward or inward relative to the equilibrium position. Figure 2 exhibits the fundamental wave formed by two intersected plane waves, where red and blue, respectively, represent peaks and troughs of the plane waves. The forward direction of the wavefront is perpendicular to the wavefront (from point  $O$  to point  $Q$  or from point  $S$  to point  $P$ ).

On the tire bead, which cannot be displaced, troughs can be reflected as peaks and vice versa. The peaks intersect on the centerline  $OP$ , which means that peaks exist on this line. Similarly, the troughs intersect to produce frontal troughs.

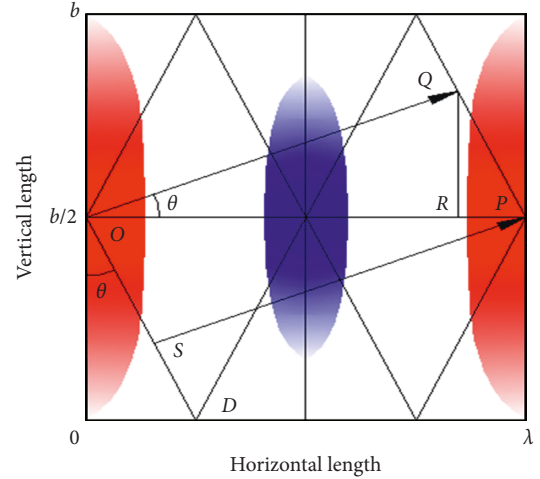


FIGURE 2: Fundamental wave formed by two intersected plane waves [10].

The darker the color, the larger the peak or trough value. The  $Y$ -axis,  $X$ -axis, and  $b$  in Figure 2 represent the vertical length, horizontal length, and tire height, respectively. The figure presents a single-period waveform, and more waveforms of other periods are distributed along the  $X$ -axis. It is shown in the figure that the displacement reaches a maximum near the centerline and approaches zero on the tire bead. The wavefront moves forward at the critical speed  $C$  within one period, with transmission distance  $OQ$ . The distance between the two peaks on the centerline represents the wavelength ( $\lambda = OP$ ). The phase velocity  $v_p$ , which refers to the transmission velocity of wave peaks along the  $X$ -axis, can be expressed as

$$v_p = \left( \frac{OP}{OQ} \right) C = \frac{C}{\cos \theta}. \quad (1)$$

Therefore,

$$\cos \theta = \frac{C}{v_p}. \quad (2)$$

The wave-group velocity  $v_g$  is the energy-flow velocity along the  $X$ -axis, and it can be expressed as

$$v_g = \left( \frac{OR}{OQ} \right) C = C \cos \theta. \quad (3)$$

The wavelength can be expressed as

$$\lambda = OP = 2b \tan \theta, \quad (4)$$

where  $\tan \theta = \sqrt{(1 - \cos^2 \theta) \cos^2 \theta}$ ,  $\tan \theta = \lambda/2b$ , and  $OD = \lambda/4$ .

Substituting  $\cos \theta = C/v_p$  into formula (4), we obtain

$$\lambda = \frac{2bv_p}{C \sqrt{1 - (C^2/v_p^2)}}. \quad (5)$$

When the tire velocity  $v_t$  and wave velocity  $v_p$  are equal in value and opposite in direction, the waves are static with regard to the tire axis, i.e., the waves are transmitted within

the tire along the direction of ground-contact points. Figure 3 demonstrates the curve of the tire centerline when the tire rotates on the drum tester at a velocity  $v_t$  that is higher than the critical speed  $C$ . Waves transmit at the velocity  $v_p$ ;  $v_p$  and  $v_t$  are equal in value and opposite in direction. The  $Y$ - and  $X$ -axes, respectively, represent the vertical and horizontal distance from the ground-contact center.

The velocity of energy flow from the ground-contact part can be expressed as

$$v_t - v_g = v_t - v_t \cos^2 \theta = v_t \left(1 - \frac{C^2}{v_t^2}\right). \quad (6)$$

The energy per unit length of oblique waves can be expressed as

$$\frac{1}{4} b \rho (\phi v_t)^2. \quad (7)$$

The tire is subjected to a vertical load and sinks so that an angle  $\phi$  is formed between the center and the edge of the ground plane, where  $\phi$  is the sinkage angle,  $v_t$  is the linear velocity of the tire, and the component of the vertical velocity of the tire is  $v_t \sin \phi$ . Since  $\phi$  is relatively small, it is reasonable to use  $\phi$  instead of  $\sin \phi$ , and the component of the vertical velocity of the tire is  $\phi v_t$ . The energy loss of a pair of waves can be expressed as

$$2(v_t - v_g) \cdot \frac{1}{4} b \rho (\phi v_t)^2 = \frac{1}{2} \phi^2 \rho b v_t (v_t^2 - C^2). \quad (8)$$

Energy consumption caused by standing waves will not occur until the tire velocity  $v_t$  exceeds the critical speed  $C$ .

### 3. Finite Element Modeling of a Radial Tire

When building a finite element model of a tire, the geometric, material, and contact nonlinearities during tire rolling may complicate the calculation process, which greatly increases computing time and convergence difficulties [10]. Therefore, under reasonable conditions, it is sensible to simplify the tire structure so that the finite element model can faithfully reflect tire deformation characteristics under various working conditions, as follows: (1) Only consider longitudinal tread grooves and ignore shallow transverse patterns, kerbing ribs, and marking lines. (2) To obtain the interactions of all parts between the tire and the road surface when analyzing the contact process, the analysis focuses on the tire crown, belt layer, and carcass layer. Therefore, there is no need to model the tire rim, which should be set as an analytical rigid body. (3) Set the road surface (test bed) as a rigid object and ignore its deformation impact on tire performance. (4) Thermal effects of air inside the tire can be ignored under static loading. The tire pressure is uniformly loaded, with evenly distributed pressure perpendicular to the inner liner [11]. The sectional structure of the tire is shown in Figure 4.

Orthogonal anisotropic materials and embedded rebar elements are used to simulate the belt and carcass layers. For stiffer ribs defined in this way, the behavior of the rubber matrix and rebar elements can be considered independent. The stiffer rib model used to define the rebar elements can

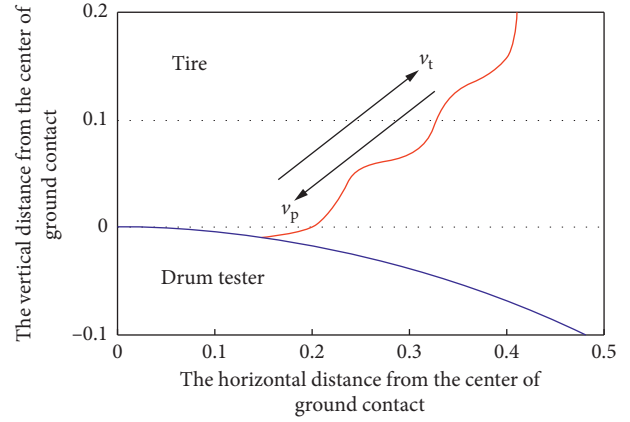


FIGURE 3: Curve of the tire centerline when  $v_t > C$  [10].

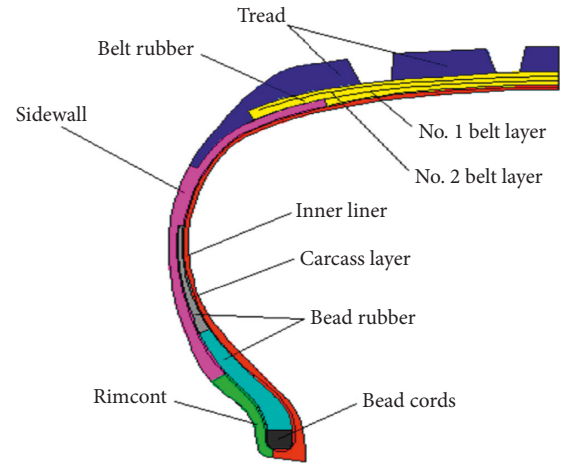


FIGURE 4: Diagram of the tire's sectional structure.

better demonstrate the stress-strain status of cords when processing the structure of the belt and the carcass layers [12]. Fine meshes are defined for cords in the first and second belt layers, as well as the carcass layer, for detailed analysis. The various rubber materials in the three-dimensional model are represented by isotropic incompressible C3D8RH elements, and the stress-strain relations of rubber materials are described with hyperelastic models [13]. The finite element model has 10,721 elements of carcass rubber and 10,102 elements in the belt and the carcass layers. Figure 5 demonstrates the finite element model of a 195/65R15 radial tire and the drum tester.

### 4. Experiment and Simulation of Mechanical Properties of the Tire

**4.1. Experiment and Simulation of Static Mechanical Properties.** A UP-2092 comprehensive test bench (Figure 6) was employed to measure the tire load-sinkage relation under standard inflation pressure (200 kPa). The tire inflatable section widths under different vertical loads were measured and compared with simulation results. The results are shown in Figure 7 and Table 1.

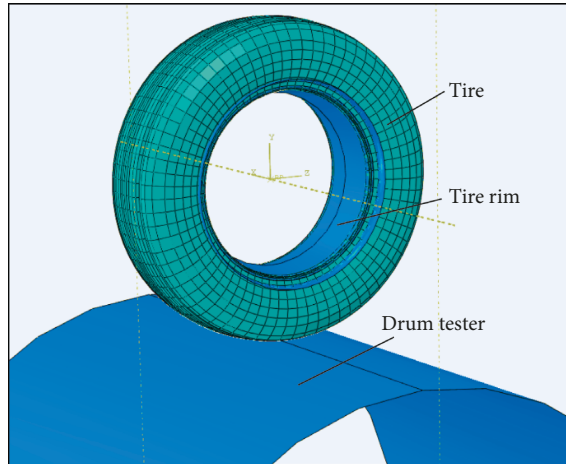


FIGURE 5: FEA modeling for the tire and the test rig.

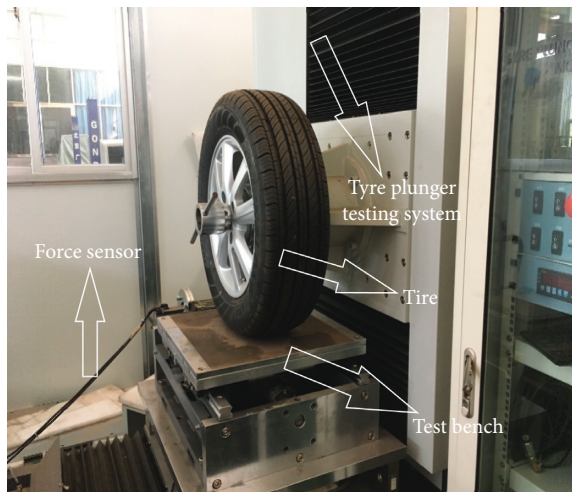


FIGURE 6: Bench test for mechanical properties of the tire.

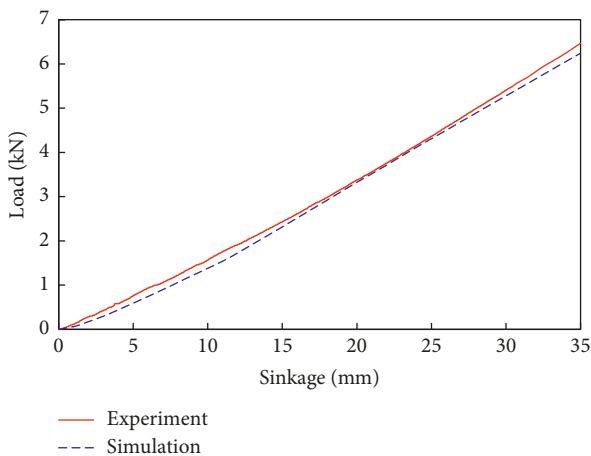


FIGURE 7: Curves of load vs sinkage by experiment and simulation.

Figure 7 shows that the simulation and experimental results are basically consistent, both indicating a linear relationship between load and sinkage. Table 1 shows that the

width of the ground-contact section increases with the load. The maximum error between simulation and experimental results is less than 2.5%; thus, the finite element model is characterized by only small errors that are within the allowable range of engineering design.

**4.2. Experiment and Simulation of Dynamic Mechanical Properties.** A tire high-speed uniformity testing machine was used to perform high-speed experiments on a 195/65R15 radial tire, with a tire pressure of 0.2 MPa and a load of 5,018 N. The tire linear velocity was gradually adjusted from 180 km/h to 230 km/h while the tire pressure and load remained unchanged. Measurements were taken at an interval of 10 km/h; images were captured by high-speed cameras and imported into CAD software to analyze standing waves on the tire surface. Since standing waves were concentrated at the rear of the ground-contact area, only the images in the concerned semicircle of the tire were selected, and the wavelengths were measured by CAD software. In addition, ABAQUS software was used for high-speed simulation of the tire with the same velocity range and boundary conditions, generating cloud images of tire deformation [14].

Figure 8 displays the comparison of experimental and simulation results on tread standing waves within the  $\pi$ -arc (images on the left are from experiments and on the right from simulation) [15]. In the simulation graph, the closer the color is to red, the greater the distortion is, and the closer the color is to blue, the smaller the distortion is. The three sidewall standing wave peaks were identified with lines coming from the tire center. The angle in the figure indicates the angle between two adjacent peaks in a period. As the rolling speed was gradually increased, the values of the two angles also increased, which means that the speed became greater, the energy consumption increased sharply, the deformation of the tire increased, and the wavelength of the sidewall gradually increased.

Figure 9 compares the wavelength curves obtained from calculations based on the oblique wave approach, experiment results, and simulation. It can be seen that the three methods show roughly the same trends, i.e., the wavelength of sidewall standing waves gradually increases with velocity.

To sum up, the simulation results are highly consistent with those from experiments under both static and dynamic conditions. In other words, the finite element model established in this paper is accurate and suitable for further simulation analysis.

## 5. Cord Stress Analysis during High-Speed Tire Rolling

High-speed tire rolling tends to damage the internal cords, causing tire bursts [8]. Stress in a radial tire is concentrated at both the turn-up point of the carcass layer and endpoints of the belt layers. When a vehicle moves, the tire sidewall is deflected from stress. Since the load is transmitted to the bead through the sidewall, the joint between the sidewall and bead is subjected to concentrated stress that may cause

TABLE 1: Section width by simulation and experiment.

Vertical load (kN)		0	1	2	3	4	5
Ground-contact section Width (mm)	Simulation	195.7	201.4	206.2	209.6	216.2	222.8
	Experiment	194.5	198.5	201.5	210.5	213.0	218.5
Error (%)		0.61	1.46	2.33	0.43	1.5	2.0

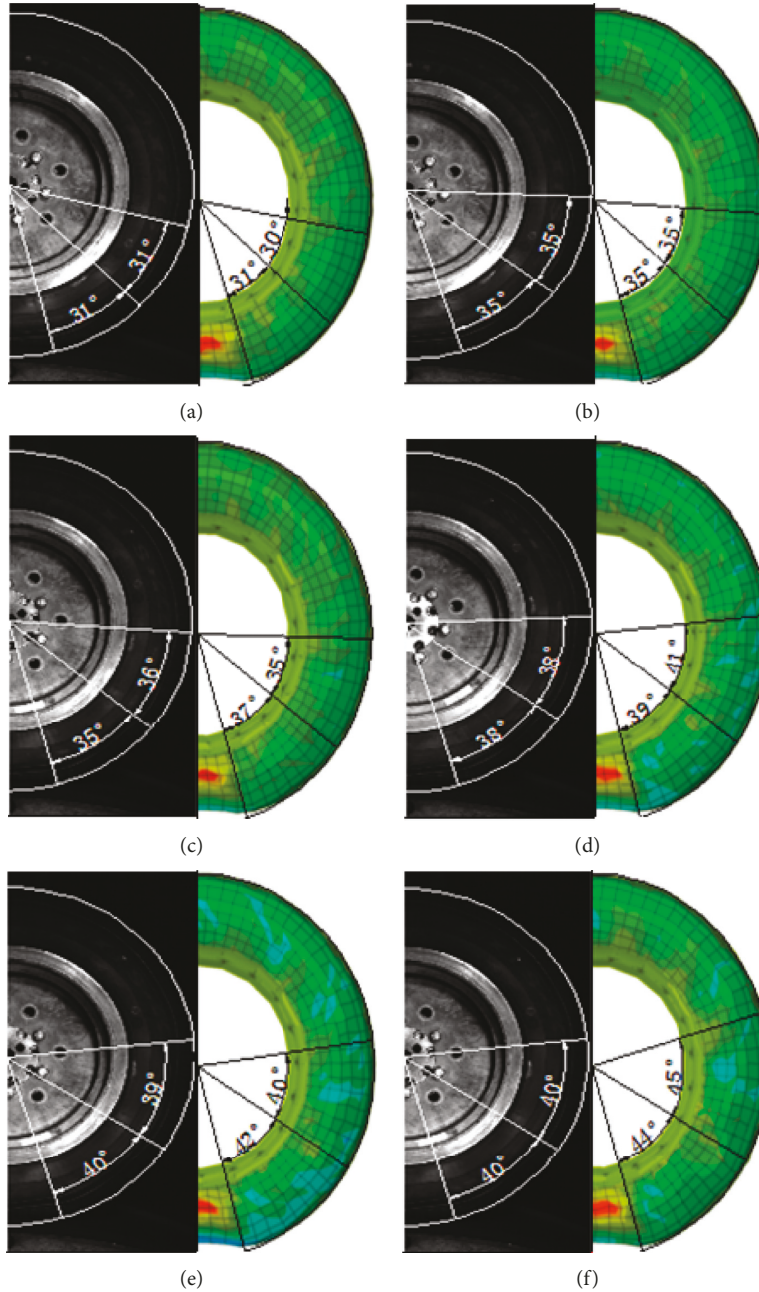


FIGURE 8: Comparison between experimental and simulated results on wavelength of standing waves within the  $\pi$ -arc at the rear of the ground-contact area at different velocities. (a) 180 km/h. (b) 190 km/h. (c) 200 km/h. (d) 210 km/h. (e) 220 km/h. (f) 230 km/h.

damage. Therefore, we selected point A on the turn-up point of the carcass layer, point B on the sidewall of the carcass layer, and points C and D, which are the cord ends of the first and second belt layers, to study the cord stress during high-speed tire rolling [16], as shown in Figure 10. The tire

pressure, load, and velocity range were set to 0.2 MPa, 5 kN, and 180–230 km/h, respectively (stress values were taken at intervals of 10 km/h). By analyzing the stress on the four points in a single rolling cycle, we can understand the stress on the tire in a free rolling cycle. During a circumferential

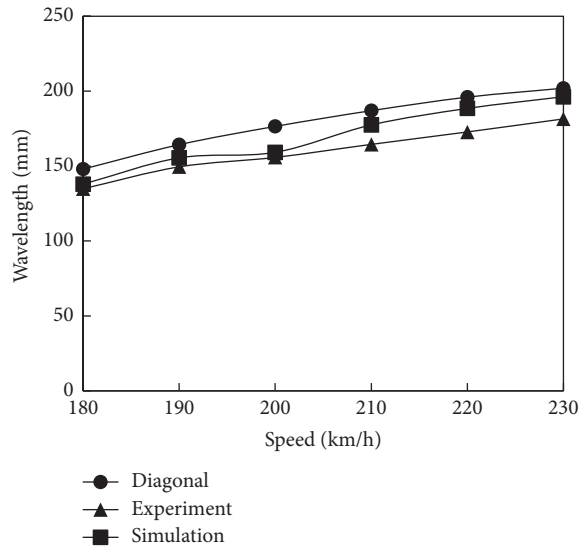


FIGURE 9: Comparison between theoretical calculation, simulation, and experiment results on wavelength of sidewall standing waves.

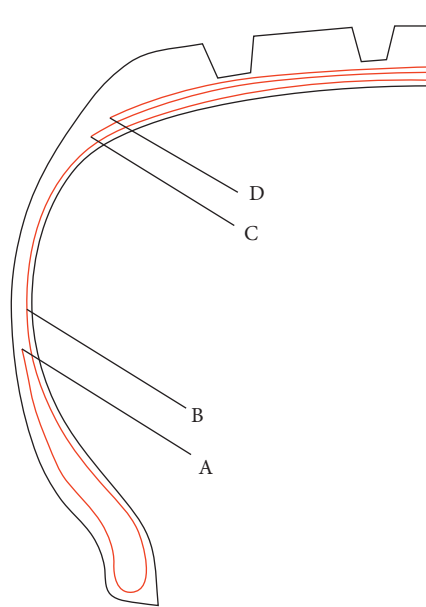


FIGURE 10: Points of circumferential analysis on cords.

cycle, the stress on the same point must have reached both the maximum and the minimum values, and the difference between the two extremes is of significance for the analysis of tire deformation and standing waves [17]. Therefore, we defined the vertex position of the tire as 0 degree, and the ground-contact center as 180 degrees [18], and we analyzed the circumferential counterclockwise cord stress on different layers during high-speed tire rolling.

**5.1. Circumferential Distribution of Carcass Cord Stress at Different Velocities.** Point A is the turn-up point of the carcass layer. The cord at this point is wrapped around the bead wire; hence, the tire sidewall deformation is constrained by the bead wire. Figures 11(a) and 11(b) show

curves of circumferential stress on points A and B, respectively, at different velocities.

As can be seen from Figure 11(a), the fluctuation amplitude of the cord stress on point A increases with velocity, and the stress reaches its maximum (about 10 N) around the ground-contact point (circumferential 180 degrees). According to previous analysis, standing waves occur during high-speed tire rolling. The wavy deformation of the tire starts at the ground-contact point (circumferential 180 degrees), moves circumferentially along the tire rotation direction, and gradually attenuates. The wavy deformation also occurs on the sidewall under the influence of standing waves, and the stress on point A changes accordingly with the standing waves. Therefore, both the wavelength of standing waves and the cord stress increase with tire velocity [19].

As can be seen from Figure 11(b), circumferential stress on point B changes wavily. Both the fluctuation amplitude and cord stress increase with velocity. The cord stress on point B reaches the minimum (about 0 N), which is insensitive to vehicle velocity, around the ground-contact point (circumferential 180 degrees). Point B is on the sidewall of the carcass layer. When standing waves are generated, there is significant deformation on the sidewall. When the maximum deformation occurs, the stress fluctuation on the sidewall reaches the peak value. The most obvious standing waves can be observed at the rear of the ground-contact point, along with bulges on the tire sidewall.

**5.2. Circumferential Stress on Belt Cord Ends at Different Velocities.** Figures 12(a) and 12(b) present circumferential stress on the cord ends C and D, respectively, at different velocities.

As shown in Figures 12(a) and 12(b), the trends of stress variation on points C and D are roughly the same: the cord stress increases with vehicle velocity and reaches its maximum around the ground-contact point. In other words, apparent asymmetric deformation occurs under the impact of ground contact. Comparing the stress on points C and D, we see that point D (the cord end of the second belt layer) is subjected to greater extreme stress (about 75 N). In addition, the cord stress fluctuates significantly at the rear of the ground-contact part, and the fluctuation amplitude increases with velocity, which is mainly attributed to the stress imbalance caused by standing waves. Therefore, in tire design, it is important to enhance the rigidity of the tire shoulder, suppress the deformation on the edge of the belt layer, and reduce the heat generated by deformation so as to prevent fatigue damage and thermal breakdown.

Through the analysis of the above four points, the regularity of the cord stress when the tire is rolling at high speed can be inferred, revealing the relationship between the stress of the cord and the standing wave, providing the research basis for the tire test mechanics. From the above four figures, it can be seen that the standing wave phenomenon will occur when the tire is rolling at a high speed. As the rolling speed increases, the amount of deformation of the tire sidewall increases, and the wavelength of the

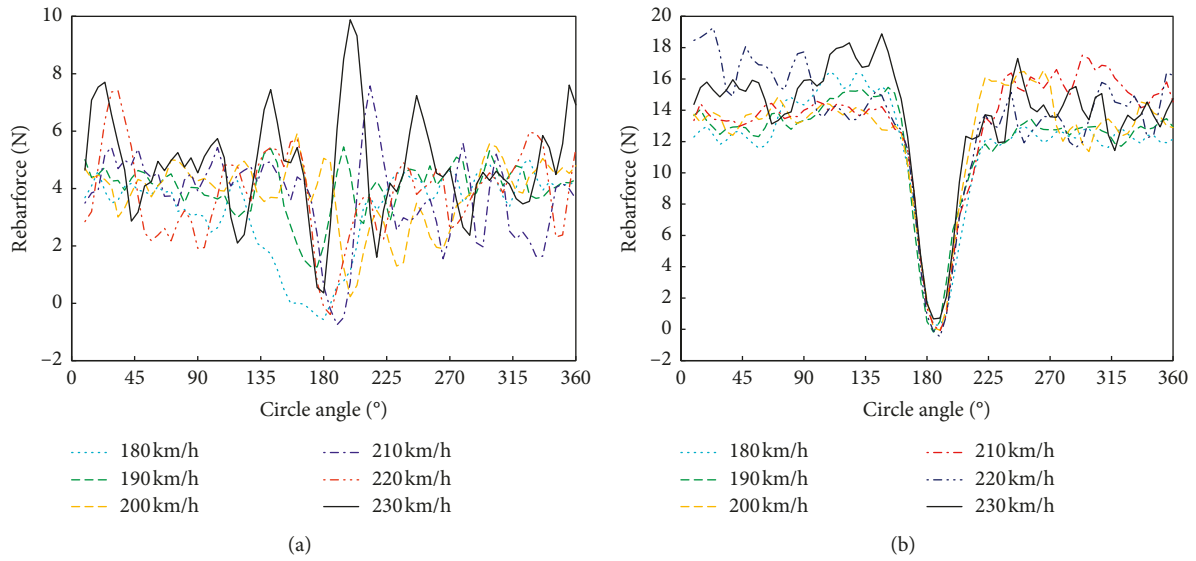


FIGURE 11: Circumferential distribution of carcass cord stress at different velocities. (a) Circumferential stress on the turn-up point of the carcass layer (point A). (b) Circumferential stress on the sidewall point of the carcass layer (point B).

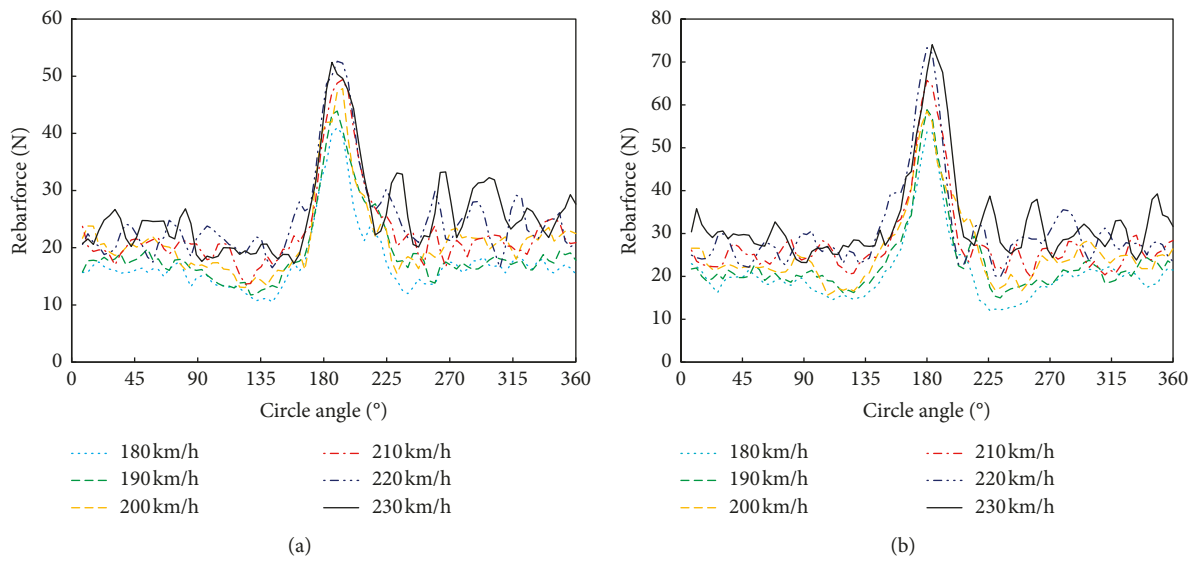


FIGURE 12: Circumferential stress on belt cord ends at different velocities. (a) Circumferential stress on the cord end of the first belt layer (point C). (b) Circumferential stress on the cord end of the second belt layer (point D).

standing wave also increases. The area where the standing wave occurs is mainly concentrated behind the grounding point, and the tire is easily damaged in this area. The higher the speed, the greater the stress of the cord and the greater the fluctuation of the curve. At this time, the tire sidewall deformation reaches the maximum, and it may bulge. Thus, when designing the structure of the tire, it is necessary to improve its shoulder rigidity and prevent the tire from damage due to deformation.

Comparing the above four figures, it can be seen that the stress of the belt cord is significantly greater than that of the ply cord, i.e., the belt cord is the main force-receiving part. Therefore, the design of the tire should aim mainly to strengthen the belt cord. Compared with the circumferential

forces of the other three points, the force fluctuation of the ply cord carcass turn-up point (point A) near the ground is less because the ply cords on the sidewall (point B) have already taken most of the force from the tire, so the force transmitted to the turn-up point A will be significantly reduced, the circumferential force at point A will be relatively even and flat, and the force at the three points of BCD will be at the grounding point, which shows greater fluctuations.

## 6. Conclusions

Using the oblique wave approach, this paper analyzes the production mechanisms of standing waves during high-

speed tire rolling, studies the relations between sidewall standing waves and vehicle velocity, and calculates the theoretical wavelengths of sidewall standing waves of a 195/65R15 radial tire. Based on the tire structure and parameters of the carcass layer and belt layers and accounting for longitudinal tire patterns, a three-dimensional finite element model of the tire was established with ABAQUS software. We compared the experimental and simulation results on the tire load-sinkage relation and load vs inflatable section width relation, and the difference between the two was found to be insignificant. High-speed experiments and simulations were carried out, with the tire load, pressure, and velocity range set to 5 kN, 0.2 Mpa, and 180–230 km/h, respectively. Images were captured at an interval of 10 km/h by CAD software. By comparing the simulation, experiment, and theoretical wavelength of standing waves, it was found that the wavelength increased with vehicle velocity. Static and dynamic simulation results from the finite element model were in good agreement with those of the experiment, which verified the accuracy of the model.

Based on this finite element model, the pattern of cord stress during high-speed tire rolling was studied by simulating the cord stress at different positions. The conclusions are as follows:

- (1) The tire rotation velocity has a significant impact on the stress at point A (the turn-up point of the carcass layer). The range of stress fluctuation increases with velocity, and the stress reaches a maximum value around the ground-contact point (circumferential 180 degrees) of the tire.
- (2) With the impact from standing waves, the cord stress on the sidewall point of the carcass layer fluctuates wavily at the rear of the ground-contact part. The higher the velocity, the greater the fluctuation amplitude and extreme cord stress. Cord stress at point B reached a minimum (0 N) around the ground-contact point.
- (3) The cord ends C and D of the first and second belt layers are subjected to similar stress conditions. As the tire velocity increases, the extreme cord stress increases accordingly, and the circumferential stress at points C and D fluctuates more significantly, particularly at the rear of the ground-contact part.
- (4) For each layer of cords inside a tire, it is generally the case that the higher the tire-rotating velocity, the greater the cord stress.

### Data Availability

The data used to support the findings of this study are available from the corresponding author upon request.

### Conflicts of Interest

The authors declare that there are no conflicts of interest regarding the publication of the article.

### Acknowledgments

This entire study was supported by the National Natural Science Foundation of China (no. 51475399), Education and Scientific Research Projects for Middle and Young-Aged Teachers of Fujian (no. JA15376), and Science & Technology Innovation Project of Fujian Province, China (no. 2016H2003).

### References

- [1] J. Padovan, "On viscoelasticity and standing waves in tires," *Tire Science and Technology*, vol. 5, no. 2, pp. 233–246, 1977.
- [2] J. R. Cho, K. W. Kim, and H. S. Jeong, "Numerical investigation of tire standing wave using 3-D patterned tire model," *Journal of Sound and Vibration*, vol. 305, no. 4–5, pp. 795–807, 2007.
- [3] R. A. Brockman, J. H. Champion, and J. P. Medzorian, "Finite element analysis of tire critical speeds," *Computers & Structures*, vol. 43, no. 3, pp. 581–593, 1992.
- [4] A. Chatterjee, J. P. Cusumano, and J. D. Zolock, "Standing waves in a simple model of a rotating balloon tire," in *Proceedings of the Recent Advances in Solids/Structures and Application of Metallic Materials ASME*, vol. 369, New Orleans, LA, USA, November 1997.
- [5] A. Chatterjee, J. P. Cusumano, and J. D. Zolock, "On contact-induced standing waves in rotating tires: experiment and theory," *Journal of Sound and Vibration*, vol. 227, no. 5, pp. 1049–1081, 1999.
- [6] Y. P. Chang, M. Ei-Gindy, and D. A. Streit, "Influence of tyre loading and inflation pressure on standing waves phenomenon using PAM-SHOCK," *International Journal of Heavy Vehicle Systems*, vol. 10, no. 1/2, p. 86, 2003.
- [7] W. Soedel, "On the dynamic response of rolling tires according to thin shell approximations," *Journal of Sound and Vibration*, vol. 41, no. 2, pp. 233–246, 1975.
- [8] S. C. Huang, "The vibration of rolling tyres in ground contact," *International Journal of Vehicle Design*, vol. 13, no. 3, pp. 78–95, 1992.
- [9] E. Vinesse and H. Nicollet, "Surface waves on the rotating tyre: an application of functional analysis," *Journal of Sound and Vibration*, vol. 126, no. 1, pp. 85–96, 1988.
- [10] D. S. Stutts and W. Soedel, "A simplified dynamic model of the effect of internal damping on the rolling resistance in pneumatic tires," *Journal of Sound and Vibration*, vol. 155, no. 1, pp. 153–164, 1992.
- [11] E. R. Gardner and T. Worswick, "Behavior of tire at high speed," *Transaction of the Proceeding of Institution of Rubber Industry*, vol. 27, no. 13, pp. 127–146, 1951.
- [12] E. Tonuk and Y. S. Unlusoy, "Prediction of automobile tire cornering force characteristics by finite element modeling and analysis," *Computers & Structures*, vol. 79, no. 13, pp. 1219–1232, 2001.
- [13] H. Bechir, L. Chevalier, and M. Idjeri, "A three-dimensional network model for rubber elasticity: the effect of local entanglements constraints," *International Journal of Engineering Science*, vol. 48, no. 3, pp. 265–274, 2010.
- [14] D. Zheng, "Prediction of tire tread wear with FEM steady state rolling contact simulation," *Tire Science and Technology*, vol. 31, no. 3, pp. 189–202, 2002.
- [15] G. R. Potts, C. A. Bell, L. T. Charek, and T. K. Roy, "Tire vibrations," *Tire Science and Technology*, vol. 5, no. 4, pp. 202–225, 1977.

- [16] N. J. Lindlsey and J. P. Cusumano, "Critical speed analysis of a non-linear strain ring dynamical model for aircraft tires," in *Proceedings of the SAE Technical Paper Series*, Colorado Springs, CO, USA, May 1993.
- [17] J. Padovan, "On viscoelasticity and standing waves in tires," *Tire Science and Technology*, vol. 4, no. 4, pp. 233–246, 1976.
- [18] J. Padovan, "On standing waves in tires," *Tire Science and Technology*, vol. 5, no. 2, pp. 83–101, 1977.
- [19] J. Padovan, A. Kasempour, F. Tabaddor, and B. Brockman, "Evaluation of critical speeds in high speed aircraft tires," in *Proceedings of the SAE Technical Paper Series*, Pittsburg, PA, USA, September 1989.

